



Altmann, Y., Pereyra, M., & McLaughlin, S. (2015). Bayesian Nonlinear Hyperspectral Unmixing With Spatial Residual Component Analysis. *IEEE Transactions on Computational Imaging*, 1(3), 174 - 185. DOI: 10.1109/TCI.2015.2481603

Publisher's PDF, also known as Version of record

License (if available):
CC BY

Link to published version (if available):
[10.1109/TCI.2015.2481603](https://doi.org/10.1109/TCI.2015.2481603)

[Link to publication record in Explore Bristol Research](#)
PDF-document

This is the final published version of the article (version of record). It first appeared online via the Institute of Electrical and Electronics Engineers at <http://dx.doi.org/10.1109/TCI.2015.2481603>.

University of Bristol - Explore Bristol Research

General rights

This document is made available in accordance with publisher policies. Please cite only the published version using the reference above. Full terms of use are available:
<http://www.bristol.ac.uk/pure/about/ebr-terms.html>

Bayesian Nonlinear Hyperspectral Unmixing With Spatial Residual Component Analysis

Yoann Altmann, *Member, IEEE*, Marcelo Pereyra, *Member, IEEE*, and Stephen McLaughlin, *Fellow, IEEE*

Abstract—This paper presents a new Bayesian model and algorithm for nonlinear unmixing of hyperspectral images. The proposed model represents the pixel reflectances as linear combinations of the endmembers, corrupted by nonlinear (with respect to the endmembers) terms and additive Gaussian noise. Prior knowledge about the problem is embedded in a hierarchical model that describes the dependence structure between the model parameters and their constraints. In particular, a gamma Markov random field is used to model the joint distribution of the nonlinear terms, which are expected to exhibit significant spatial correlations. An adaptive Markov chain Monte Carlo algorithm is then proposed to compute the Bayesian estimates of interest and perform Bayesian inference. This algorithm is equipped with a stochastic optimisation adaptation mechanism that automatically adjusts the parameters of the gamma Markov random field by maximum marginal likelihood estimation. Finally, the proposed methodology is demonstrated through a series of experiments with comparisons using synthetic and real data and with competing state-of-the-art approaches.

Index Terms—Hyperspectral imagery, nonlinear spectral unmixing, residual component analysis, Gamma Markov random field, Bayesian estimation.

I. INTRODUCTION

SPECTRAL unmixing (SU) is a key problem in the analysis of hyperspectral images. This is a source separation problem consisting of recovering the spectral signatures (endmembers) of the materials present in the scene, and quantifying their proportions within each hyperspectral image pixel. The SU problem has been widely studied for images where pixel reflectances are linear combinations of pure component spectra [1], [2]. However, it is now widely accepted that the linear mixing model (LMM) can be inappropriate for some hyperspectral images, particularly those containing sand-like materials or relief. Several nonlinear mixing models (NLMM) have been recently proposed to address the limitations of the LMM. There are two main approaches to dealing with NLMM. The first

seeks to model the physics of the image formation model (e.g., *intimate mixtures* [3] for short-range multiple light scattering, and polynomial models for long-range multiple light scattering [4]–[7]). The second seeks to construct flexible models that can represent a wide range of nonlinearities. This can be achieved using neural networks, kernel functions [8], or post-nonlinear transformations [9], [10] for instance.

While the consideration of nonlinear effects can be very relevant in some specific regions of the scene, most hyperspectral image pixels are well described by the LMM. Therefore, models for nonlinear unmixing should include the LMM as a special case. Here we use a variation of the Bayesian NLMM proposed recently in Altmann et al. [11], which is inspired by residual component analysis (RCA) [12]. In that model the nonlinear effects in hyperspectral images are represented as additive perturbations (of the LMM) that are modelled as a collection of Gaussian processes (GPs) combined with a hidden Potts-Markov random field (MRF) partitioning the image into regions sharing the same GP. The model of [11] has two drawbacks that we address in this paper. First, the Potts model leads to a piecewise constant representation that constrains nonlinearities to take a finite number of possible energy states (the so-called *nonlinearity levels*); this number is difficult to specify a priori unless there is very accurate knowledge about the nonlinearities present in the scene. Second, in [11] nonlinearities are allowed to take negative values, as this allows marginalising them analytically (i.e., integrating them out of the model) and thus simplifies the statistical inference procedure;. However, our experiments suggest that taking into account the assumption that the nonlinearities are positive can improve the estimation results significantly when the nonlinear terms are positive (see [7] for more details about this positivity assumption). Here we address these drawbacks by replacing the Potts MRF by a gamma MRF model [13]. This model has the key advantages of 1) promoting spatial regularity in the nonlinearity terms without enforcing a piecewise constant representation with a finite number of levels, and 2) it can easily incorporate a positivity constraint for the nonlinearities.

The remainder of the paper is organised as follows. Section II recalls the RCA model for hyperspectral image unmixing. The Bayesian NLMM proposed in this paper is presented in Section III. In Section IV we propose a Markov chain Monte Carlo Bayesian algorithm to perform statistical inference in this model and we define Bayesian estimators for nonlinear unmixing and nonlinearity detection. Sections V and VI demonstrate the proposed methodology through a series of experiments with synthetic and real hyperspectral images and comparisons with methods from the state of the art. Conclusions and perspectives for future work are finally reported in Section VII.

Manuscript received September 15, 2015; accepted September 15, 2015. Date of publication September 23, 2015; date of current version October 26, 2015. This work was supported in part by the Direction Générale de l'armement, French Ministry of Defence, in part by the SuStaIN program—EPSRC under Grant EP/D063485/1—at the Department of Mathematics, University of Bristol, and in part by the EPSRC under Grant EP/J015180/1. The associate editor coordinating the review of this paper and approving it for publication was Dr. William Clem Karl.

Y. Altmann and S. McLaughlin are with the School of Engineering and Physical Sciences, Heriot-Watt University, Edinburgh EH14 4AS, U.K. (e-mail: Y.Altmann@hw.ac.uk; S.McLaughlin@hw.ac.uk).

M. Pereyra is with the School of Mathematics, University of Bristol, Bristol BS8 1TW, U.K. (e-mail: marcelo.pereyra@bristol.ac.uk).

Color versions of one or more of the figures in this paper are available online at <http://ieeexplore.ieee.org>.

Digital Object Identifier 10.1109/TCI.2015.2481603

II. PROBLEM FORMULATION

Let $\mathbf{y}_{i,j} \in \mathbb{R}^L$ be the pixel at location (i, j) of an hyperspectral image \mathbf{Y} of size $N_{\text{row}} \times N_{\text{col}}$ and observed at L spectral bands. We model each image pixel as a linear combination of R known spectra or endmembers \mathbf{m}_r , plus an additive perturbation $\phi_{i,j}$ embedding nonlinearities and additive noise

$$\begin{aligned} \mathbf{y}_{i,j} &= \sum_{r=1}^R a_{r,i,j} \mathbf{m}_r + \phi_{i,j} + \mathbf{e}_{i,j} \\ &= \mathbf{M} \mathbf{a}_{i,j} + \phi_{i,j} + \mathbf{e}_{i,j}, \quad \forall (i, j) \end{aligned} \quad (1)$$

where $\mathbf{m}_r = [m_{r,1}, \dots, m_{r,L}]^T$ is the spectral response of the r th material present in the scene, $a_{r,i,j}$ is its abundance within pixel (i, j) and $\mathbf{e}_n \sim \mathcal{N}(\mathbf{0}_L, \boldsymbol{\Sigma}_0)$ is Gaussian noise with diagonal covariance matrix $\boldsymbol{\Sigma}_0 = \text{diag}(\boldsymbol{\sigma}^2)$ with elements $\boldsymbol{\sigma}^2 = [\sigma_1^2, \dots, \sigma_L^2]^T$ (note that matrix and vector notations $\mathbf{M} = [\mathbf{m}_1, \dots, \mathbf{m}_R]$ and $\mathbf{a}_{i,j} = [a_{1,i,j}, \dots, a_{R,i,j}]^T$ have been used in the second row of (1)). Due to physical considerations we model the abundances as non-negative quantities and set $a_{r,i,j} \in \mathbb{R}^+$ (notice that because we consider non-linear mixing we do not use the sum-to-one constraint that is commonly enforced in linear mixing models). Moreover, for the nonlinear effects we use the deterministic model

$$\begin{aligned} \phi_{i,j} = \phi(\boldsymbol{\gamma}_{i,j}) &= \sum_{k=1}^{R-1} \sum_{k'=k+1}^R \gamma_{i,j}^{(k,k')} \sqrt{2} \mathbf{m}_k \odot \mathbf{m}_{k'} \\ &+ \sum_{k=1}^R \gamma_{i,j}^{(k)} \mathbf{m}_k \odot \mathbf{m}_k. \end{aligned} \quad (2)$$

that is parametrised by a vector of nonlinearity coefficients $\boldsymbol{\gamma}_{i,j} = [\gamma_{i,j}^{(1,2)}, \dots, \gamma_{i,j}^{(R-1,R)}, \gamma_{i,j}^{(1)}, \dots, \gamma_{i,j}^{(R)}]^T$ of length $K = R(R+1)/2$. This choice of model is motivated by the fact that the nonlinearities in hyperspectral images are well modelled by polynomial interactions between endmembers, which provides a flexible representation that can approximate a wide range of nonlinear effects (see [5]–[7], [9], [14] for more details). Moreover, in this paper we assume that $\gamma_{i,j} \in \mathbb{R}^+$ because of the considerations reported in [7] and because we have observed that it can improve estimation results significantly. However, in Section V we also describe a version of our model where this positivity constraint is relaxed. Also note that the factors $\sqrt{2}$ in (2) are simply introduced to simplify kernel computations [9], however these factors do not have a physical interpretation and can be removed from (2) without changing the model by scaling the coefficients $\gamma_{i,j}^{(k,k')}$ appropriately.

This paper considers the inverse problems of estimating the abundances $\mathbf{a}_{i,j}$ and of detecting the presence of nonlinearities at each image pixel $\mathbf{y}_{i,j}$ (whose intensity can then be measured by estimating $\|\boldsymbol{\gamma}_{i,j}\|_2^2$). We formulate this problem as a statistical inference task that we address in a Bayesian framework by defining an appropriate Bayesian model and inference algorithm.

III. BAYESIAN MODEL

This section presents an original Bayesian model for inferring the unknown quantities of interest \mathbf{A} and $\boldsymbol{\Gamma}$ from the

observed hyper-spectral image \mathbf{Y} , where \mathbf{A} is an $R \times N_{\text{row}} \times N_{\text{col}}$ array gathering the abundance vectors $\mathbf{a}_{i,j}$ and $\boldsymbol{\Gamma}$ an $K \times N_{\text{row}} \times N_{\text{col}}$ array gathering the nonlinearity coefficient vectors $\boldsymbol{\gamma}_{i,j}$. Following a hierarchical Bayesian approach, we also include in the model all the parameters of the model whose values are not easily known a priori and need to be inferred from data jointly with \mathbf{A} and $\boldsymbol{\Gamma}$ (e.g., the noise covariance $\boldsymbol{\sigma}^2$). Unlike \mathbf{A} and $\boldsymbol{\Gamma}$, the other unknown quantities are of no interest for decision making and are therefore removed from the model by marginalisation during the inference procedure.

A. Likelihood

From the non-linear mixing model (1), and by assuming that observations $\mathbf{Y} = [\mathbf{y}_1, \dots, \mathbf{y}_N]$ are conditionally independent given $\mathbf{A}, \boldsymbol{\Gamma}$ and $\boldsymbol{\sigma}^2$, we obtain

$$\begin{aligned} f(\mathbf{Y} | \mathbf{A}, \boldsymbol{\Gamma}, \boldsymbol{\sigma}^2) \\ \propto \prod_{i,j} |\boldsymbol{\Sigma}_0|^{-1/2} \exp \left[-\frac{(\mathbf{y}_{i,j} - \mathbf{x}_{i,j})^T \boldsymbol{\Sigma}_0^{-1} (\mathbf{y}_{i,j} - \mathbf{x}_{i,j})}{2} \right] \end{aligned} \quad (3)$$

with $\mathbf{x}_{i,j} = \mathbf{M} \mathbf{a}_{i,j} + \phi(\boldsymbol{\gamma}_{i,j})$, $\boldsymbol{\Sigma}_0 = \text{diag}(\boldsymbol{\sigma}^2)$, and where \propto denotes proportionality. Note that to lighten notation the dependence on \mathbf{M} is not denoted explicitly (\mathbf{M} is assumed to be perfectly known).

B. Prior for the abundance matrix \mathbf{A}

We assign the abundance coefficients the following hierarchical prior distribution

$$\begin{aligned} a_{r,i,j} | \beta_r &\sim \mathcal{N}_{\mathbb{R}^+}(0, \beta_r) \\ \beta_r &\sim \mathcal{IG}(\alpha_1, \alpha_2) \end{aligned} \quad (4)$$

parametrised by some fixed hyper-parameters α_1 and α_2 , and where $\mathcal{N}_{\mathbb{R}^+}(0, \beta_r)$ denotes the truncated Gaussian distribution on \mathbb{R}^+ with mode 0 and scale parameter $\beta_r^{1/2}$, reflecting the positivity of $a_{r,i,j}$. This prior model is very flexible and can be adjusted to represent a wide variety of prior beliefs. Without loss of generality, here we set $\alpha_1 = 1$ and $\alpha_2 = 2$, leading to a (marginal) exponential prior for $a_{r,i,j}$ that represents our prior beliefs that abundances are proportions and take values mainly in $[0, 1]$. In particular that we expect small values to occur more frequently because most materials are not present on all image pixels (notice however that the exact values of α_1 and α_2 generally have little impact on the inference because \mathbf{A} is very high dimensional and dominates the distribution of β_r).

A strength of hierarchical priors such as (4) is their natural capacity to encode prior dependences between unknown variables. For example, we expect the abundance coefficients associated with the same material to exhibit correlations, particularly in terms of their scale. This belief is encoded in (4) by defining one common hidden variable β_r for each material or endmember \mathbf{m}_r , which is shared by all the abundances related to that material. This hierarchical structure operates as a global pooling mechanism that shares information across the rows of

\mathbf{A} (i.e, the abundance coefficients associated to the r th material) to improve estimation performance. It is also possible to relate (4) to a group ℓ_1 regularisation or a composite $\ell_1 - \ell_2$ regularisation, in the sense that without the pooling mechanism marginalising the hidden variables β_r would lead to an ℓ_1 regularisation for the abundances $a_{r,i,j}$, and introducing the pooling mechanism also links the rows of \mathbf{A} at the level of their ℓ_2 norms. Finally, it is also worth mentioning that model (4) does not account explicitly for spatial correlations between the abundance vectors. This information could be introduced into the model by using mixtures of Gaussian or Dirichlet distributions [15], [16]. However, the main focus of this paper is the consideration of the spatial dependence between the nonlinearities and their impact on estimation performance, though we hope and anticipate that future models will exploit both types of spatial information.

Finally, assuming that abundances are prior independent given the hidden variables $\beta = [\beta_1, \dots, \beta_R]^T$, we obtain the following joint prior for \mathbf{A}, β

$$f(\mathbf{A}, \beta) = f(\mathbf{A}|\beta)f(\beta) \quad (5)$$

with $f(\mathbf{A}|\beta) = \prod_{r,i,j} f(a_{r,i,j}|\beta_r)$ and $f(\beta) = \prod_r f(\beta_r|\alpha_1, \alpha_2)$. Also notice that by using the hierarchical structure (4) we obtain conjugate priors and hyper-priors for $a_{r,i,j}$ and β_r . Conjugacy generally leads to inference algorithms with significantly better tractability and computational efficiency, which is crucial given the high dimensionality of \mathbf{A} .

C. Priors for the nonlinearity coefficients Γ

One of the contributions of this paper is to propose the following hierarchical prior for the nonlinearity coefficients

$$\begin{cases} \gamma_{i,j}|s_{i,j} \sim \mathcal{N}_{\mathbb{R}_+^K}(\mathbf{0}, s_{i,j}\mathbf{I}_K) \\ s_{i,j} \sim \mathcal{IG}(\alpha_3, \alpha_3\alpha_{4,i,j}) \end{cases} \quad (6)$$

where \mathbb{R}_+^K denotes the K -dimensional positive orthant, reflecting a positivity constraint on $\gamma_{i,j}$. Notice that this prior is parametrised by a local hyper-parameter $\alpha_{4,i,j}$ that is related to the prior mean of $s_{i,j}$, and therefore to the average power of the nonlinearities at the pixel (i, j) (via the norm $\|\gamma_{i,j}\|_2^2$). The prior also depends on a global hyper-parameter α_3 that controls the shape of the tails of the prior (6), and therefore the probability of large deviations between $s_{i,j}$ and $\alpha_{4,i,j}$. A careful selection of $\alpha_{4,i,j}$ and α_3 will allow exploiting the spatial dependences between the nonlinearity coefficients $\gamma_{i,j}$ to improve estimation performance.

As explained previously, a key feature of hierarchical models is their capacity to encode dependences and act as pooling mechanisms that share information across covariates to improve the inference. Here we wish to specify (6) to reflect the prior belief that nonlinearities exhibit spatial correlations. In particular, due to the spatial organisation of images, we expect the values of $\gamma_{i,j}$ to vary smoothly from one pixel to another and exhibit occasional abrupt and sharp changes. In order to model this behaviour we specify $\alpha_{4,i,j}$ such that the resulting prior for Γ is a hidden gamma-Markov random field (GMRF) [13]. More precisely, we denote by \mathbf{S} the $N_{\text{row}} \times N_{\text{col}}$ matrix with

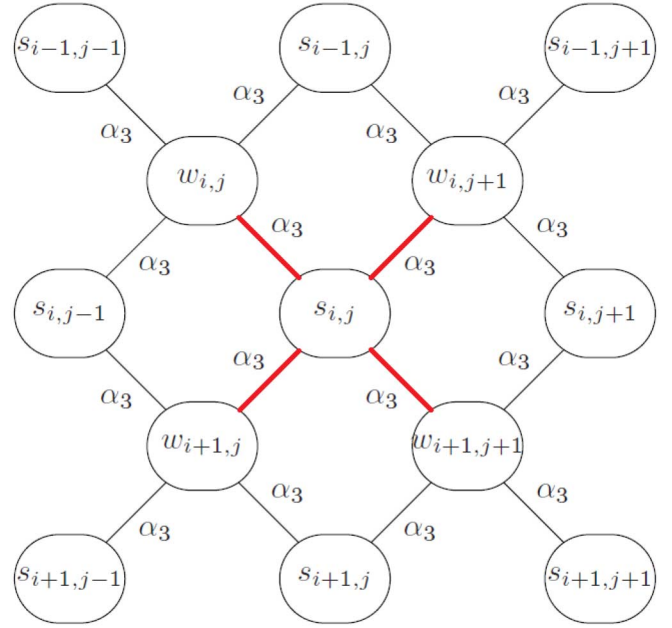


Fig. 1. Proposed 1st order neighbourhood structure ($\forall(i, j) \in \Omega$).

elements $s_{i,j}$, introduce a $(N_{\text{row}} + 1) \times (N_{\text{col}} + 1)$ auxiliary matrix \mathbf{W} with elements $w_{i,j} \in \mathbb{R}^+$ and define a bipartite conditional independence graph between \mathbf{S} and \mathbf{W} such that each $s_{i,j}$ is connected to four neighbour elements of \mathbf{W} and vice-versa. This 1st order neighbourhood structure is depicted in Fig. 1., where we notice that any given $s_{i,j}$ and $s_{i+1,j}$ are 2nd order neighbours via $w_{i,j+1}$ and $w_{i+1,j+1}$. The role of these auxiliary variables is to introduce positive dependence between the neighbouring elements of $s_{i,j}$ and therefore to promote regularity. However, this model also allows occasional sharp changes because the distribution of any $s_{i,j}$ given its neighbours in $s_{i+1,j}$ is heavy-tailed. A GMRF prior for \mathbf{S}, \mathbf{W} [13] is then defined as the following hierarchical prior [13]:

$$\gamma_{i,j}|s_{i,j} \sim \mathcal{N}_{\mathbb{R}_+^K}(\mathbf{0}, s_{i,j}\mathbf{I}_K) \quad (7a)$$

$$s_{i,j}|\mathbf{W}, \alpha_3 \sim \mathcal{IG}(\alpha_3, \alpha_3\alpha_{4,i,j}(\mathbf{W})) \quad (7b)$$

$$w_{i,j}|\mathbf{S}, \alpha_3 \sim \mathcal{G}(\alpha_3, 1/(\alpha_3\alpha_{5,i,j}(\mathbf{S}))) \quad (7c)$$

where

$$\alpha_{4,i,j}(\mathbf{W}) = w_{i,j} + w_{i+1,j} + w_{i,j+1} + w_{i+1,j+1}/4$$

$$\alpha_{5,i,j}(\mathbf{W}) = (s_{i,j}^{-1} + s_{i-1,j}^{-1} + s_{i,j-1}^{-1} + s_{i-1,j-1}^{-1})/4.$$

The density for this joint prior for Γ, \mathbf{S} and \mathbf{W} is given by

$$f(\Gamma, \mathbf{S}, \mathbf{W}|\alpha_3) = f(\Gamma|\mathbf{S})f(\mathbf{S}, \mathbf{W}|\alpha_3)$$

where $f(\Gamma|\mathbf{S}) = \prod_{i,j} f(\gamma_{i,j}|s_{i,j})$ and

$$\begin{aligned} f(\mathbf{S}, \mathbf{W}|\alpha_3) &= \frac{1}{Z(\alpha_3)} \prod_{(i,j) \in \mathcal{V}_{\mathbf{S}}} (s_{i,j})^{-(\alpha_3+1)} \\ &\times \prod_{(i',j') \in \mathcal{V}_{\mathbf{W}}} w_{i',j'}^{(\alpha_3-1)} \\ &\times \prod_{((i,j),(i',j')) \in \mathcal{E}} \exp\left(\frac{-\alpha_3 w_{i',j'}}{4s_{i,j}}\right). \end{aligned} \quad (8)$$

Notice that we denote explicitly the dependence on the value of α_3 , which here acts a regularisation parameter that controls the amount of spatial smoothness enforced by the GMRF. Following an empirical Bayesian approach, the value of α_3 remains unspecified and will be adjusted automatically during the inference procedure by maximum marginal likelihood estimation using the technique [17]. We refer to this model as *gamma-RCA* with positivity constraint (G-RCA+).

Finally, it is worth mentioning that this model for the non-linearity coefficients has similarities with the model proposed in [11] that also considers the spatial regularity of non-linearities. However, the model described [11] follows a segmentation approach in which the non-linearity coefficients are assumed to (and constrained) to take values in a finite set of possible values. This leads to a piece-wise constant representation and requires specification of the number of nonlinearity levels present in the image, a value that is often difficult to determine a priori. The model proposed in this paper provides a spatially smooth representation of the nonlinearities that is possibly more realistic than the piece-wise constant representation of [11], and also has the practical advantage of not requiring practitioners to specify the finite number of admissible nonlinearity levels. Another important distinction is that the model described in [11] does not allow the non-negativity constraint for $\gamma_{i,j}$ to be introduced, which we have found to improve significantly the estimation of the nonlinearities when the nonlinear coefficients (see [7] for more details about this positivity assumption).

For potential applications where the assumption of positive nonlinear terms would not hold, the proposed model G-RCA+ can be modified to allow $\gamma_{i,j}$ to take positive and negative values in \mathbb{R} by using the following hierarchical prior

$$\gamma_{i,j}|s_{i,j} \sim \mathcal{N}(\mathbf{0}, s_{i,j}\mathbf{I}_K) \quad (9a)$$

$$s_{i,j}|\mathbf{W}, \alpha_3 \sim \mathcal{IG}(\alpha_3, \alpha_3\alpha_{4,i,j}(\mathbf{W})) \quad (9b)$$

$$w_{i,j}|\mathbf{S}, \alpha_3 \sim \mathcal{G}(\alpha_3, 1/(\alpha_3\alpha_{5,i,j}(\mathbf{S}))). \quad (9c)$$

Notice that now $\gamma_{i,j}|s_{i,j}$ is Gaussian, instead of truncated Gaussian as in (7a). This modification leads to a gamma-RCA model without positive constraint (G-RCA) that bridges between the proposed G-RCA+ model and the original RCA model [11], where nonlinearity coefficients are constrained to take a finite number of positive and negative values. For brevity, we henceforth consider the G-RCA+ model unless stated otherwise.

D. Prior for the noise covariance σ^2

We assume that there is no prior knowledge available about the values of noise covariance (other than the fact that it is diagonal) and assign each diagonal element σ_ℓ^2 a Jeffreys' prior, leading to the joint prior

$$f(\sigma^2) = \prod_{\ell=1}^L f(\sigma_\ell^2), \quad \text{with } f(\sigma_\ell^2) \propto \sigma_\ell^{-2} \mathbf{1}_{\mathbb{R}^+}(\sigma_\ell^2). \quad (10)$$

In scenarios where prior knowledge is available, practitioners can incorporate this information into the model by replacing the Jeffreys' prior by a more informative model (e.g. a conjugate inverse-Gamma distribution).

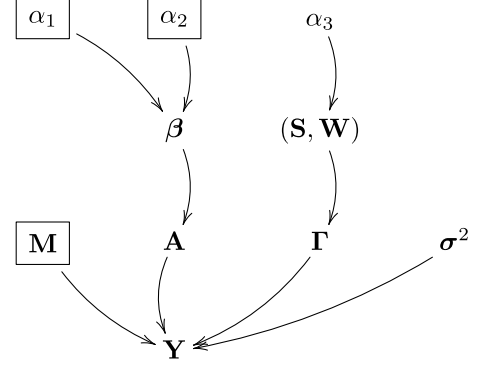


Fig. 2. Graphical model for the proposed hierarchical Bayesian model (fixed quantities appear in boxes).

E. Posterior distribution

We are now ready to specify the posterior distribution for $\mathbf{A}, \Gamma, \sigma^2, \mathbf{S}, \mathbf{W}$ and β given the observed hyper-spectral image \mathbf{Y} and the value of the spatial regularisation hyper-parameter α_3 (recall that this value will be determined by maximum marginal likelihood estimation during the inference procedure). Using Bayes' theorem, and assuming prior independence between (\mathbf{A}, β) , $(\Gamma, \mathbf{S}, \mathbf{W})$ and σ^2 , the joint posterior distribution associated with the proposed Bayesian model is given by

$$f(\mathbf{A}, \Gamma, \sigma^2, \mathbf{S}, \mathbf{W}, \beta | \mathbf{Y}, \alpha_3) \propto f(\mathbf{Y} | \mathbf{A}, \Gamma, \sigma^2) f(\mathbf{A} | \beta) f(\beta) f(\Gamma | \mathbf{S}) f(\mathbf{S}, \mathbf{W} | \alpha_3). \quad (11)$$

For illustration, Fig. 2. depicts the directed acyclic graph (DAG) summarising the structure proposed Bayesian model (recall that \mathbf{S}, \mathbf{W} have a bi-partite neighbourhood structure, which is illustrated in the graphical model of Fig. 1).

IV. BAYESIAN INFERENCE

A. Bayesian estimators

The Bayesian model defined in Section III specifies the joint posterior density for the unknown parameters $\mathbf{A}, \Gamma, \sigma^2, \mathbf{S}, \mathbf{W}$ and β given the observed quantities \mathbf{Y}, \mathbf{M} and the hyper-parameter α_3 . This posterior distribution models our complete knowledge about the unknowns given the observed data and the prior information available. In this section we define suitable Bayesian estimators to summarise this knowledge and perform hyperspectral unmixing. More precisely, we propose the following two Bayesian estimators for hyperspectral non-linear unmixing and nonlinearity estimation and detection: The marginal posterior mean or minimum mean square error estimator of the abundance matrix

$$\hat{\mathbf{A}}_{\text{MMSE}} = \mathbb{E}[\mathbf{A} | \mathbf{Y}, \hat{\alpha}_3], \quad (12)$$

where the expectation is taken with respect to the marginal posterior density $f(\mathbf{A} | \mathbf{Y}, \alpha_3)$ (by marginalising $\Gamma, \sigma^2, \mathbf{S}, \mathbf{W}$ and β this density takes into account their uncertainty). The

minimum mean square error estimator of the pixel-wise nonlinearity energy

$$\left(\widehat{\|\phi_{i,j}\|_2^2} \right)_{\text{MMSE}} = \mathbb{E} [\|\phi_{i,j}\|_2^2 | \mathbf{Y}, \hat{\alpha}_3], \quad (13)$$

where the expectation is now taken with respect to the marginal posterior density $f(\|\phi_{i,j}\|_2^2 | \mathbf{Y}, \alpha_3)$. And the Bayesian hypothesis test for nonlinearity detection

$$P_{i,j} > a_1 / (a_0 + a_1),$$

where

$$P_{i,j} = \mathbb{E} [T_{i,j}(\phi_{i,j}, \mathbf{a}_{i,j}) > \eta | \mathbf{Y}, \hat{\alpha}_3], \quad (14)$$

with

$$T_{i,j}(\phi_{i,j}, \mathbf{a}_{i,j}) = \frac{\|\phi_{i,j}\|_2^2}{\|\mathbf{y}_{i,j} - \mathbf{M}\mathbf{a}_{i,j} - \phi_{i,j}^{(t)}\|_2^2},$$

is the posterior probability that the power of the nonlinear effects in pixel (i, j) is η times larger than the power of the noise at that pixel, and where a_0 and a_1 are application-specific weights associated with incorrectly rejecting or accepting this hypothesis (in our experiments we have used $a_0 = a_1, \eta = 2$).

Notice that in (12), (13) and (14) we have set $\alpha_3 = \hat{\alpha}_3$, which denotes the maximum marginal likelihood estimator of the MRF regularisation hyper-parameter α_3 given the observed data \mathbf{Y} , i.e.,

$$\hat{\alpha}_3 = \underset{\alpha_3 \in \mathbb{R}^+}{\operatorname{argmax}} f(\mathbf{Y} | \alpha_3), \quad (15)$$

This approach for specifying α_3 is taken from the empirical Bayes framework in which hyper-parameters with unknown values are replaced by point estimates computed from observed data (as opposed to being fixed a priori or integrated out of the model by marginalisation). As explained in [17], this strategy has several important advantages for MRF hyper-parameters with doubly intractable conditional distributions such as α_3 . In particular, it allows for the automatic adjustment of the value of α_3 for each image (thus producing significantly better estimation results than using a single fixed value of α_3 for all images), and has a computational cost that is several times lower than that of competing approaches, such as including α_3 in the model and subsequently marginalising it during the inference procedure [18].

B. Bayesian algorithm

Computing the estimators (12), (13) and (14) is very challenging because it involves calculating expectations with respect to posterior marginal densities, which in turn require evaluating the full posterior (11) and integrating it over a very high-dimensional space. Computing $\hat{\alpha}_3$ is also difficult because it involves solving an intractable optimisation problem, (because it is not possible to evaluate the marginal likelihood $f(\mathbf{Y} | \alpha_3)$ or its gradient $\nabla f(\mathbf{Y} | \alpha_3)$). Here we adopt the approach proposed in [17] and design a stochastic optimisation and simulation algorithm to compute (12), (13), (14) and

(11) simultaneously. That is, we construct a stochastic gradient Markov chain Monte Carlo (SGMCMC) algorithm that simultaneously estimates $\hat{\alpha}_3$ and generates a chain of N_{MC} samples $\{\mathbf{A}^{(t)}, \mathbf{\Gamma}^{(t)}, \mathbf{S}^{(t)}\}_{t=1}^{N_{\text{MC}}}$ asymptotically distributed according to the marginal density $f(\mathbf{A}, \mathbf{\Gamma}, \mathbf{S} | \mathbf{Y}, \hat{\alpha}_3)$ (this algorithm is summarised in Algo. 1 below). Once the samples have been generated, the estimators (12), (13) and (14) are approximated by Monte Carlo integration [19, Chap. 10], i.e.,

$$\hat{\mathbf{A}}_{\text{MMSE}j} = \frac{1}{N_{\text{MC}} - N_{\text{bi}}} \sum_{t=N_{\text{bi}}+1}^{N_{\text{MC}}} \mathbf{A}^{(t)}, \quad (16)$$

$$\left(\widehat{\|\phi_{i,j}\|_2^2} \right)_{\text{MMSE}j} = \frac{1}{N_{\text{MC}} - N_{\text{bi}}} \sum_{t=N_{\text{bi}}+1}^{N_{\text{MC}}} \left\| \phi(\gamma_{i,j}^{(t)}) \right\|_2^2, \quad (17)$$

and

$$\hat{P}_{i,j} = \frac{1}{N_{\text{MC}} - N_{\text{bi}}} \sum_{t=N_{\text{bi}}+1}^{N_{\text{MC}}} \left[\mathbf{1}_{(\eta, \infty)} \left(T_{i,j}^{(t)} \right) \right], \quad (18)$$

with $T_{i,j}^{(t)} = \|\phi(\gamma_{i,j}^{(t)})\|_2^2 / \|\mathbf{y}_{i,j} - \mathbf{M}\mathbf{a}_{i,j} - \phi(\gamma_{i,j}^{(t)})\|_2^2$, and where the samples from the first N_{bi} iterations (corresponding to the transient regime or burn-in period) are discarded. The main steps of this algorithm are detailed in below.

Algorithm 1. Proposed MCMC algorithm

- 1: **Fixed input parameters:** Endmember matrix \mathbf{M} , number of burn-in iterations N_{bi} , total number of iterations N_{MC}
 - 2: **Initialization ($t = 0$)**
 - Set $\mathbf{A}^{(0)}, \boldsymbol{\sigma}^{2(0)}, \mathbf{\Gamma}^{(0)}, \mathbf{S}^{(0)}, \mathbf{W}^{(0)}, \boldsymbol{\beta}^{(0)}, \alpha_3^{(0)}$
 - 3: **Iterations ($1 \leq t \leq N_{\text{MC}}$)**
 - 4: Sample $(\mathbf{A}^{(t)}, \mathbf{\Gamma}^{(t)})$ from (20) if using G-RCA+, or Sample $(\mathbf{A}^{(t)}, \mathbf{\Gamma}^{(t)})$ from (22) if using G-RCA
 - 5: Sample $\boldsymbol{\sigma}^{2(t)}$ from (23)
 - 6: Sample $\boldsymbol{\beta}^{(t)}$ from (25)
 - 7: Sample $\mathbf{S}^{(t)}$ from (26)
 - 8: Sample $\mathbf{W}^{(t)}$ from (7c)
 - 9: **if** $t < N_{\text{bi}}$ **then**
 - 10: Sample $(\mathbf{S}', \mathbf{W}') \sim \mathcal{K}(\mathbf{S}, \mathbf{W} | \mathbf{S}^{(t)}, \mathbf{W}^{(t)}, \alpha_3^{(t-1)})$
 - 11: Set $\alpha_3^{(t)} = \mathcal{P}_{[0, A_t]}(\alpha_3^{(t-1)} + \delta_t [\Lambda(\mathbf{S}, \mathbf{W}) - \Lambda(\mathbf{S}', \mathbf{W}')])$
with $\Lambda(\mathbf{S}, \mathbf{W}) = - \sum_{((i,j), (i',j')) \in \mathcal{E}} \frac{w_{i',j'}}{s_{i,j}} + 4 \left(\sum_{(i',j') \in \mathcal{V}_{\mathbf{W}}} \log(w_{i',j'}) - \sum_{(i,j) \in \mathcal{V}_{\mathbf{S}}} \log(s_{i,j}) \right)$
 - 12: **else**
 - 13: Set $\alpha_3^{(t)} = \alpha_3^{(t-1)}$
 - 14: **end if**
 - 15: Set $t = t + 1$.
 - 16: Output $\{\mathbf{A}^{(t)}, \mathbf{\Gamma}^{(t)}, \mathbf{S}^{(t)}\}_{t=1}^{N_{\text{MC}}}$.
-

1) *Sampling the mixing parameters:* The conditional distribution of $\mathbf{A}, \mathbf{\Gamma}$ given the other variables of the model is given by

$$f(\mathbf{A}, \mathbf{\Gamma} | \mathbf{Y}, \boldsymbol{\Psi}, \boldsymbol{\sigma}^2, \alpha_3) = \prod_{i,j} f(\mathbf{a}_{i,j}, \gamma_{i,j} | \mathbf{y}_n, \boldsymbol{\Psi}, \boldsymbol{\sigma}^2) \quad (19)$$

where

$$\mathbf{a}_{i,j}, \gamma_{i,j} | \mathbf{y}_n, \Psi, \sigma^2 \sim \mathcal{N}_{\mathbb{R}^R + \mathbb{K}}(\boldsymbol{\mu}_{i,j}, \boldsymbol{\Sigma}_{i,j}), \quad (20)$$

with

$$\begin{cases} \boldsymbol{\Sigma}_{i,j} = (\mathbf{R}_{i,j} + \mathbf{G}^T \boldsymbol{\Sigma}_0^{-1} \mathbf{G})^{-1}, \\ \boldsymbol{\mu}_{i,j} = \boldsymbol{\Sigma}_{i,j} \mathbf{G}^T \boldsymbol{\Sigma}_0^{-1} \mathbf{y}_{i,j}, \end{cases} \quad (21)$$

and where \mathbf{G} is an $L \times (R + D)$ matrix with the endmembers and the D nonlinear interaction spectra, i.e., $\mathbf{G} = [\mathbf{M}, \mathbf{m}_1 \odot \mathbf{m}_2, \dots, \mathbf{m}_{R-1} \odot \mathbf{m}_R, \mathbf{m}_1 \odot \mathbf{m}_1, \dots, \mathbf{m}_R \odot \mathbf{m}_R]$ and

$$\mathbf{R}_{i,j} = \left(\begin{bmatrix} \text{diag}(\boldsymbol{\beta}) & \mathbf{0}_{R,D} \\ \mathbf{0}_{D,R} & s_{i,j} \mathbf{I}_D \end{bmatrix} \right)^{-1}.$$

We simulate from (20) using the method proposed in [20]. Moreover, for the G-RCA model that does not constrain $\gamma_{i,j}$ to be positive, we replace (20) with the alternative conditional distribution for $\mathbf{a}_{i,j}, \gamma_{i,j} | \mathbf{y}_n, \Psi, \sigma^2$ given by

$$\mathbf{a}_{i,j}, \gamma_{i,j} | \mathbf{y}_n, \Psi, \sigma^2 \sim \mathcal{N}_{\mathbb{R}_+^R \times \mathbb{R}^{\mathbb{K}}}(\boldsymbol{\mu}_{i,j}, \boldsymbol{\Sigma}_{i,j}), \quad (22)$$

that is also easy to sample using the method proposed in [20].

2) *Sampling the noise variances:* The conditional distribution of σ^2 given the other variables of the model is given by

$$\begin{aligned} f(\sigma^2 | \mathbf{Y}, \mathbf{A}, \boldsymbol{\Gamma}, \Psi, \alpha_3) \\ = \prod_{\ell=1}^L f(\sigma_\ell^2 | \mathbf{Y}, \mathbf{A}, \Psi, \boldsymbol{\beta}, \alpha_3), \end{aligned} \quad (23)$$

with

$$\begin{aligned} f(\sigma_\ell^2 | \mathbf{Y}, \mathbf{A}, \boldsymbol{\Gamma}, \mathbf{S}, \mathbf{W}, \boldsymbol{\beta}, \alpha_3) \\ = p_{\text{IG}} \left(\sigma_\ell^2; N/2, \sum_{i,j} \frac{(\mathbf{y}_{i,j} - \mathbf{x}_{i,j})^T \boldsymbol{\Sigma}_0^{-1} (\mathbf{y}_{i,j} - \mathbf{x}_{i,j})}{2} \right). \end{aligned} \quad (24)$$

Sampling from the conditional (23) is achieved by simulating L independent inverse gamma random variables.

3) *Sampling the abundance hyper-parameters:* Similarly, the elements of $\boldsymbol{\beta}$ are also conditionally independent (given the other variables of the model) and can be simulated in parallel by generating inverse gamma random variables with distribution

$$\beta_r | \mathbf{Y}, \boldsymbol{\theta}, \mathbf{S}, \mathbf{W}, a \sim \text{IG} \left(\frac{N}{2} + \alpha_1, \sum_{i,j} \frac{\mathbf{a}_{i,j}^2}{2} + \alpha_2 \right). \quad (25)$$

4) *Sampling the nonlinearity levels \mathbf{S} :* Again, the elements of \mathbf{S} are conditionally independent given the other model parameters

$$\begin{aligned} f(\mathbf{S} | \mathbf{Y}, \boldsymbol{\theta}, \mathbf{W}, \alpha_3) \\ = \prod_{(i,j) \in \mathcal{V}_S} f(s_{i,j} | \mathbf{Y}, \boldsymbol{\theta}, \mathbf{W}, \alpha_3), \end{aligned} \quad (26)$$

and can be simulated in parallel by generating inverse gamma random variables with distribution

$$s_{i,j} | \mathbf{Y}, \boldsymbol{\theta}, \mathbf{W}, \alpha_3 \sim \text{IG} \left(\alpha_3 + \frac{K}{2}, \nu_{i,j} + \frac{\|\gamma_{i,j}\|_2^2}{2} \right). \quad (27)$$

5) *Updating the MRF regularisation parameter α_3 :* If marginal likelihood $f(\mathbf{Y} | \alpha_3)$ was tractable we could update α_3 from one MCMC iteration to the next by using a classic gradient descent step

$$\alpha_3^{(t+1)} = \alpha_3^{(t)} + \delta_t \nabla \log f(\mathbf{Y} | \alpha_3^{(t)}),$$

with $\delta_t = t^{-3/4}$, such that $\alpha_3^{(t)}$ converges to $\hat{\alpha}_3$ as $t \rightarrow \infty$. However, this gradient has two levels of intractability, one due to the marginalisation of $(\mathbf{A}, \boldsymbol{\Gamma}, \sigma^2, \mathbf{S}, \mathbf{W}, \boldsymbol{\beta})$ and another one due to the intractable normalising constant of the gamma MRF. We address this difficulty by following the approach proposed in [17]; that is, by replacing $\nabla \log f(\mathbf{Y} | \alpha_3^{(t)})$ with an estimator computed with the samples generated by the MCMC algorithm at iteration t , and a set of two auxiliary variables $(\mathbf{S}', \mathbf{W}') \sim \mathcal{K}(\mathbf{S}, \mathbf{W} | \mathbf{S}^{(t)}, \mathbf{W}^{(t)}, \alpha_3^{(t-1)})$ generated with an MCMC kernel \mathcal{K} with target density (8) (in our experiments we used a Gibbs sampler implemented using a colouring scheme such that all the elements of \mathbf{S}' and \mathbf{W}' are generated in parallel). The updated value $\alpha_3^{(t+1)}$ is then projected onto an interval $[0, A_t]$ to guarantee the positivity constraint $\alpha_3 \in \mathbb{R}^+$ and the stability of the stochastic optimisation algorithm (we have used $A_t = 20$).

It is worth mentioning that if it was possible to simulate the auxiliary variables $(\mathbf{S}', \mathbf{W}')$ exactly from (8) then the estimator of $\nabla \log f(\mathbf{Y} | \alpha_3^{(t)})$ used in Algo. 1 would be unbiased and as a result $\alpha_3^{(t)}$ would converge exactly to $\hat{\alpha}_3$. However, exact simulation from (8) is not computationally feasible and therefore we resort to the MCMC kernel \mathcal{K} and obtain a biased estimator of $\nabla \log f(\mathbf{Y} | \alpha_3^{(t)})$ that drives $\alpha_3^{(t)}$ to a neighbourhood of $\hat{\alpha}_3$ [17]. We have found that computing this biased estimator is significantly less expensive than alternative approaches, (e.g., using an approximate Bayesian computation algorithm as in [18]), and that it leads to very accurate nonlinear unmixing results.

V. SIMULATIONS: SYNTHETIC DATA

In this section we study the performance of the proposed algorithm on a series of synthetic hyperspectral images firstly with linear mixing and secondly with nonlinear mixing.

A. First scenario: Linearly mixed image

The objective here is to assess whether using the nonlinear unmixing model proposed in this paper leads to good unmixing results when analysing linearly mixed images, or if the additional degrees of freedom in the model degrade the estimation performance. This is crucial because in real hyperspectral images most pixels exhibit predominantly linear mixing. We evaluate the performance of the proposed G-RCA algorithm (and its version incorporating the nonlinearity positivity constraints, G-RCA+) by unmixing a synthetic image of 100×100 pixels generated with the classical linear mixing model (i.e., (1) with $\gamma_{i,j} = 0$) and using $R = 3$ endmembers (i.e., green grass, olive green paint and galvanised steel metal)¹. This image

¹We extracted these endmembers from the spectral libraries of the ENVI software [21] in a similar fashion to previous work [6], [9], [22].

is generated using $L = 207$ spectral bands uniformly sampled from 400 nm to 2500 nm and with an average signal to noise ratio of 30 dB ($\sigma_\ell^2 = 3.10^{-4}, \forall \ell$). The abundance vectors $\mathbf{a}_{i,j}$ used to produce this image have been generated using the model (4) (we later present another experiment where the abundances satisfy the sum-to-one constraint). The G-RCA and G-RCA+ algorithms for this experiment were implemented with $N_{MC} = 2000$, $N_{bi} = 1500$.

The performance unmixing algorithms in terms of abundance estimation is evaluated by computing the root normalised mean square error (RNMSE) defined by

$$\text{RNMSE} = \sqrt{\frac{1}{N_{\text{row}}N_{\text{col}}R} \sum_{i,j} \|\mathbf{a}_{i,j} - \hat{\mathbf{a}}_{i,j}\|^2} \quad (28)$$

where $\mathbf{a}_{i,j}$ and $\hat{\mathbf{a}}_{i,j}$ are the true and estimated abundance vectors for the pixel (i, j) of the image.

For this scenario, the proposed G-RCA algorithm is compared with the classical NCLS algorithm [1] assuming the LMM (without sum-to-one constraint (STO)), comparisons to nonlinear SU methods will be addressed in scenario 2 described below. The results obtained with G-RCA, G-RCA+ and NCLS are 1.04×10^{-2} , 1.04×10^{-2} and 0.97×10^{-2} respectively. We observe that the three methods performed similarly, showing that using G-RCA+ to analyse linearly mixed pixels does not degrade significantly the estimation performance.

By analysing the distribution of the estimated nonlinearity levels $\hat{s}_{i,j}^2$ (computed by approximating the expectation $E[s_{i,j}^2 | \mathbf{Y}, \hat{\alpha}_3]$) we confirm that G-RCA/G-RCA+ correctly identifies linearly mixed pixels. Indeed, the mean and variance of the estimated nonlinearity levels (computed by polling the 10000 pixels) are 1.4×10^{-4} and 1.9×10^{-7} for G-RCA and 2.0×10^{-5} and 4.2×10^{-9} for G-RCA+, confirming that the amplitude of the nonlinear coefficients are significantly smaller than that of the abundances. It is also worth mentioning that unlike NCLS, G-RCA/G-RCA+ is able to handle unknown coloured noise (i.e., frequency-dependent noise levels).

B. Second scenario: Nonlinear mixtures

Data Set: The objective here is to evaluate the performance of the proposed model when applied to images containing different kinds of linear and nonlinear mixtures. We consider a synthetic image of 100×100 pixels generated with the same $R = 3$ endmembers of the previous experiment, but using 6 different mixing models. More precisely, we have used a Potts-Markov random field (with parameter $\beta = 1.6$) to generate a spatially coherent partition of the image where each partition is assigned to one of the 6 mixing models, which was then used to generate the observations for that partition of the image, (the map with the mixing model assigned to each pixel is depicted in Fig. 3(a)). The class \mathcal{C}_1 (resp. \mathcal{C}_2) is associated the LMM without (resp. with) abundance STO (LMM-WSTO and LMM-STO, respectively). The pixels of class \mathcal{C}_3 have been

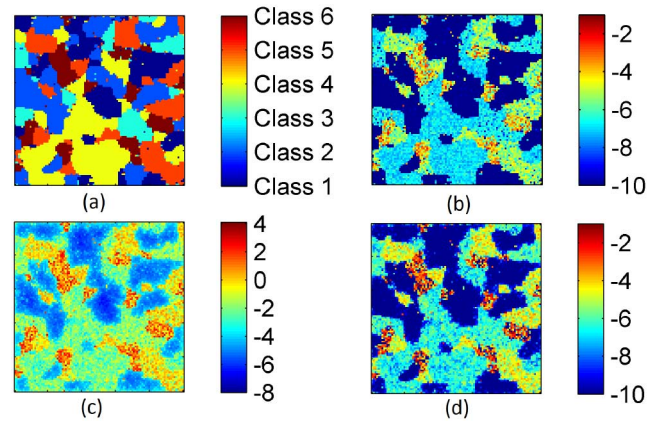


Fig. 3. Nonlinear unmixing: (a) Mixing model (class) allocation, (b) true log-energy of the nonlinear effects, (c)-(d) nonlinear log-energy estimated with G-RCA and with G-RCA+.

generated according to the generalized bilinear mixing model (GBM) [6]

$$\mathbf{y}_{i,j} = \sum_{r=1}^R a_{r,i,j} \mathbf{m}_r + \sum_{k=1}^{R-1} \sum_{k'=k+1}^R \gamma_{i,j}^{(k,k')} a_{k,i,j} a_{k',i,j} \mathbf{m}_k \odot \mathbf{m}_{k'} + \mathbf{e}_{i,j} \quad (29)$$

with $\gamma_{i,j}^{(k,k')} = 1$, which corresponds to the model investigated in [14] (Fan's model). The class \mathcal{C}_4 is composed of pixels generated according to the PPNMM [9] as follows

$$\mathbf{y}_{i,j} = \mathbf{M} \mathbf{a}_{i,j} + b (\mathbf{M} \mathbf{a}_{i,j}) \odot (\mathbf{M} \mathbf{a}_{i,j}) + \mathbf{e}_{i,j}. \quad (30)$$

with $b = 0.2$. The pixels of the class \mathcal{C}_5 have been generated using the bilinear model investigated in [5], referred to as Nascimento's model (NM) and defined as

$$\mathbf{y}_{i,j} = \sum_{r=1}^R a_{r,i,j} \mathbf{m}_r + \sum_{k=1}^{R-1} \sum_{k'=k+1}^R \gamma_{i,j}^{(k,k')} \mathbf{m}_k \odot \mathbf{m}_{k'} + \mathbf{e}_{i,j} \quad (31)$$

where the mixture coefficients (associated with the linear and nonlinear terms) of each pixel sum to one. Finally, the class \mathcal{C}_6 has been generated according to (1) with zero-mean Gaussian nonlinearity coefficients with variance $s_{i,j}^2 = 0.1$. Note that \mathcal{C}_6 is the only class allowing for negative nonlinearities. For the classes \mathcal{C}_2 , \mathcal{C}_3 and \mathcal{C}_4 (whose underlying models rely on the abundance STO assumption), the abundance vectors have been randomly generated according to a uniform distribution over the admissible set defined by the positivity and sum-to-one constraints. The mixing coefficients in (31) (for the pixels of \mathcal{C}_5) have been uniformly generated in the simplex defined by the positivity and STO constraints. The abundances of the pixels in \mathcal{C}_1 and \mathcal{C}_6 have been generated according to (4) with $\beta_r = 0.3, \forall r$. All pixels have been corrupted by additive i.i.d Gaussian noise of variance $\sigma^2 = 3 \times 10^{-4}$, corresponding to an

TABLE I
SCENARIO 2: ABUNDANCE RNMSEs ($\times 10^{-2}$)

		\mathcal{C}_1 (LMM-WSTO)	\mathcal{C}_2 (LMM-STO)	\mathcal{C}_3 (GBM)	\mathcal{C}_4 (PPNM)	\mathcal{C}_5 (NM)	\mathcal{C}_6 (RCA)
SU Algo.	NLCS	0.98	0.96	5.11	5.10	10.38	26.35
	FLCS	81.45	0.59	11.57	9.90	32.51	30.40
	GBM	80.68	0.60	4.64	5.01	32.54	29.25
	PPNM	70.33	1.11	1.85	0.97	28.13	23.08
	NM	81.06	0.98	11.53	9.77	2.73	29.43
	RCA	1.12	1.09	2.69	2.62	3.63	6.85
	G-RCA	1.34	1.29	2.69	2.65	3.56	6.96
	G-RCA+	1.21	1.14	2.11	2.86	2.88	19.63

average signal-to-noise ratio SNR 29 dB. The noise is assumed to be i.i.d. for a fair comparison with SU algorithms assuming i.i.d. Gaussian noise. Fig. 3(b) shows the log-energy of the nonlinear contribution for each pixel of the image, i.e., $\log(\phi_{i,j})$.

Unmixing: Different estimation procedures have been considered for the four different mixing models:

- The NCLS algorithm [1] which is known to have good performance for linear mixtures when the abundance STO assumption can be relaxed.
- The FCLS algorithm [1] which is known to have good performance for linear mixtures and relying on the abundance STO.
- The GBM-based optimization approach [6] which is adapted for bilinear nonlinearities. The optimization algorithm is stopped when the norm of the difference between consecutive parameter estimates is smaller than 10^{-6} .
- The gradient-based approach of [9] which is based on a PPNM and has shown nice properties for various polynomial nonlinearities.
- The FCLS algorithm used with an extended endmember matrix (containing the bilinear products of the endmembers) for unmixing based on the NM. This algorithm is denoted by NM in the remainder of the paper.
- The RCA algorithm proposed in [11] with $K = 6$ classes, $N_{MC} = 3000$, $N_{bi} = 200$ and $\beta = 1.6$ (β is the granularity parameter of the Potts model used in [11] for nonlinearity-based segmentation).
- The proposed G-RCA/G-RCA+ with $N_{MC} = 2000$, $N_{bi} = 1500$.

The abundance estimation performance of 6 unmixing strategies is evaluated using the RNMSE obtained for each class of pixels and defined by

$$\text{RNMSE}_k = \sqrt{\frac{1}{N_k R} \sum_{(i,j) \in I_k} \|\mathbf{a}_{i,j} - \hat{\mathbf{a}}_{i,j}\|^2} \quad (32)$$

where I_k is the set of indices of the pixels in the class \mathcal{C}_k and N_k is the number of pixels in \mathcal{C}_k . The results obtained by the 6 algorithms and are presented in Table I which shows that the model (1)–(2) leads to robust abundance estimation algorithms since all RCA, G-RCA and G-RCA+ provide satisfactory results for the 6 different mixtures. Moreover, we observe that G-RCA+ and G-RCA perform almost as well as RCA; note that G-RCA+ and G-RCA are fully unsupervised, whereas RCA requires

specification of the parameters K and β (note that the results in Table I have been obtained with the best values for K and β identified by cross-validation, using different values could have degraded estimation performance significantly). We also observe that G-RCA+ generally provides better abundance estimates than G-RCA, supporting the assumption that $\gamma_{i,j} \in \mathbb{R}^+$. Finally, Fig. 3, (c) and (d) show the nonlinearity level map estimated by G-RCA and G-RCA+ (computed from the estimates of $\{\|\phi_{i,j}\|^2\}$). We observe that both G-RCA+ and G-RCA were able to correctly identify the regions where nonlinear effects occur, and that G-RCA+ produced a better estimate of the nonlinearity energies.

In order to assess the capacity of GRCA+ and GRCA to fits different types of mixing models, Table II reports the average image reconstruction (RE) for each class of pixels and defined by

$$\text{RE}_k = \sqrt{\frac{1}{N_k L} \sum_{(i,j) \in I_k} \|\mathbf{y}_{i,j} - \hat{\mathbf{y}}_{i,j}\|^2} \quad (33)$$

where $\hat{\mathbf{y}}_{i,j}$ is the (i,j) th reconstructed pixel. The reconstruction errors in Table II confirm that RCA and G-RCA are very flexible and can handle the 6 different mixing models associated with the 6 classes considered. More precisely, the reconstruction errors provided by RCA and G-RCA correspond to the standard deviation of the additive Gaussian noise ($\sigma^2 = 3 \times 10^{-4}$). G-RCA+ also provides accurate reconstructions errors, except for class \mathcal{C}_6 , because G-RCA+ does not consider negative nonlinearities.

Bayesian detection of nonlinearity As explained previously, the proposed MCMC algorithm can be used to detect image pixels with significant nonlinear mixing (this is formulated as a Bayesian hypothesis test involving the posterior probability (14)). In order to illustrate this, Fig. 4 compares the true nonlinearity presence map (depicted in Fig. 4(a)) with the probabilities (18) estimated with G-RCA+ and $\eta = 2$ (Fig. 4(b)) and the corresponding detection map (Fig. 4(c)) for the synthetic image considered in Scenario 2. Recall that the detection map is computed by thresholding the probability map (we used $a_0 = a_1$ leading to a threshold value of 0.5). It is worth noting that both η in (14) and the loss function coefficients a_0, a_1 are application specific and can be adjusted to reflect prior knowledge about the confidence in the model for a specific scene, the probability of nonlinear effects, and the relative cost of false positive (false alarm) and false negative detections. Moreover,

TABLE II
SCENARIO 2: RECONSTRUCTION ERRORS ($\times 10^{-2}$)

		C_1 (LMM-WSTO)	C_2 (LMM-STO)	C_3 (GBM)	C_4 (PPNM)	C_5 (NM)	C_6 (RCA)
SU Algo.	NLCS	1.72	1.72	1.81	1.78	2.07	4.43
	FLCS	55.12	1.72	2.61	2.49	7.65	11.69
	GBM	54.54	1.72	1.92	2.01	7.65	11.28
	PPNM	9.47	1.72	1.73	1.72	3.26	4.00
	NM	55.09	1.73	2.62	2.62	1.71	9.97
	RCA	1.72	1.71	1.70	1.71	1.70	1.70
	G-RCA	1.72	1.71	1.70	1.71	1.70	1.70
	G-RCA+	1.72	1.72	1.72	1.72	1.72	3.60

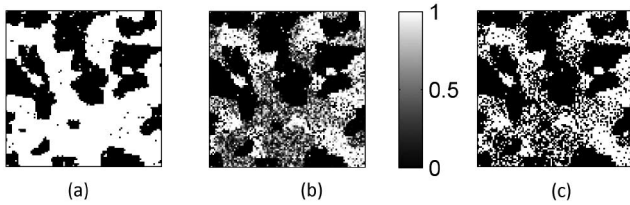


Fig. 4. Nonlinear mixing detection in the synthetic image of Scenario 2: (a) Nonlinearity presence/absence (ground truth), (b) Posterior probability of significant nonlinearities $P_{i,j}$ estimated with G-RCA+ using (14), (c) Bayesian hypothesis test for nonlinearity detection ($P_{i,j} > 1/2$).

TABLE III
SCENARIO 2: DETECTION PERFORMANCE

	$\eta = 1$	$\eta = 1.5$	$\eta = 2$	$\eta = 2.5$	$\eta = 3$
$P_{FA}(\times 10^{-2})$	0.53	0.15	0.30	0.02	0
$P_D(\times 10^{-2})$	85.83	78.93	72.33	66.15	60.95

Table III shows the the empirical probability of false alarm P_{FA} and probability of detection P_D computed with G-RCA+ for this experiment and using different values of η . We observe the good performance of G-RCA+, which for $\eta = 1$ is able to detect over 85% of nonlinearly mixed pixels with a probability of false alarm of 0.5%. Finally, it is of note that unlike the original RCA algorithm [11], the Bayesian model proposed in this paper does not allocate prior probability to the specific case of linearly mixed pixels (i.e., the case $\phi_{i,j} = \mathbf{0}$ has prior density but not prior mass). As a result, it is not possible to perform Bayesian point hypothesis tests (i.e., $\phi_{i,j} = \mathbf{0}$ vs $\phi_{i,j} \neq \mathbf{0}$) that are possible with RCA. The development of a new Bayesian model and Bayesian tests that combine the strengths of both approaches is currently under investigation.

VI. SIMULATIONS: REAL HYPERSPECTRAL IMAGE

This section presents an application of the proposed G-RCA method to a real hyperspectral image. The hyperspectral image considered in this experiment was acquired in 2010 by the Hypspec hyperspectral scanner over Villelongue, France ($00^\circ 03'W$ and $42^\circ 57'N$). This scene was observed at $L = 160$ spectral bands ranging from the visible to near infra-red with a spatial resolution of 0.5 m. This dataset has already been studied in [10], [11], [23], [24] and is mainly composed of forested and urban areas (see [23] for more details about the data acquisition and pre-processing steps). We have applied our

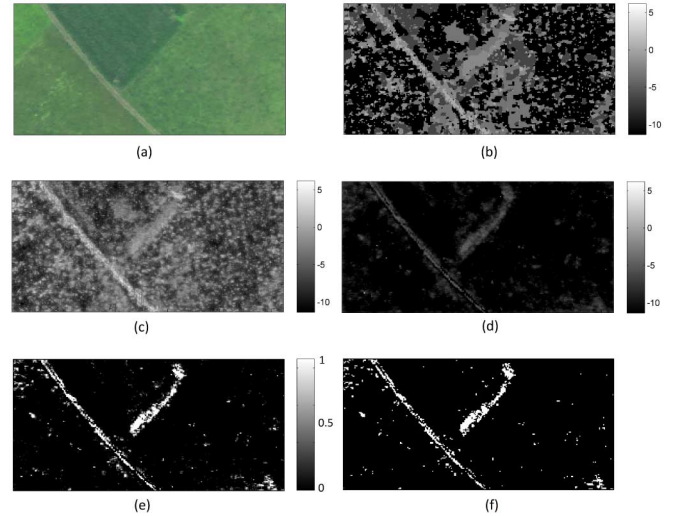


Fig. 5. Nonlinearity level estimation: (a) True colour image of the scene of interest. Levels of nonlinearity estimated with RCA (using $K = 5$ levels) (b), with G-RCA (c) and with G-RCA+ (d). (e) G-RCA+ estimation of posterior probability of significant nonlinear mixing (14) ($\eta = 2$), and (f) nonlinear mixing detection map.

method to the region of interest of size 180×250 pixels that is depicted in Fig. 5(a). This region is composed mainly of a path and different vegetation species and has $R = 5$ endmembers, whose spectral signatures have been extracted from the data using VCA [25].

Figs. 5(c) and (d) show the nonlinearity levels estimated with the proposed G-RCA/G-RCA+ method. For comparison, the results obtained with RCA [11] are presented in Fig. 5(d) (recall that to simplify the estimation problem, RCA artificially constrains nonlinearities to take a finite number of values (5 here)). Since RCA does not directly estimate $\{\|\phi_{i,j}\|^2\}$ but $\{\|s_{i,j}\|^2\}$, Figs. 5(c) and (d) depicts the minimum mean square error estimator of the pixel-wise nonlinearity level

$$\hat{S}_{MMSE} = E[S|\mathbf{Y}, \hat{\alpha}_3], \quad (34)$$

where the expectation is now taken with respect to the marginal posterior density $f(S|\mathbf{Y}, \alpha_3)$. In a similar fashion to the abundance estimators, these estimators are approximated using Monte Carlo using

$$\hat{S}_{MMSEj} = \frac{1}{N_{MC} - N_{bi}} \sum_{t=N_{bi}+1}^{N_{MC}} \mathbf{S}^{(t)}. \quad (35)$$

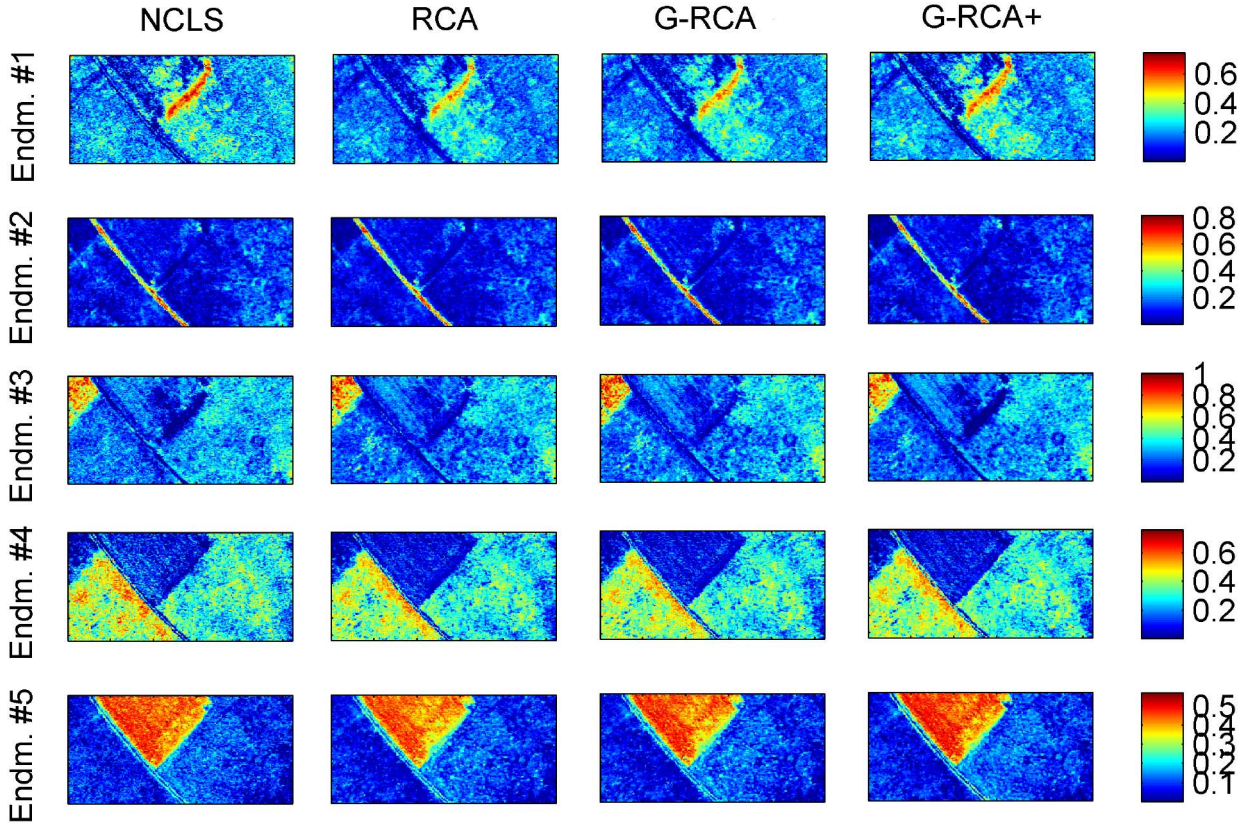


Fig. 6. Abundance maps estimated with NCLS, RCA, G-RCA and G-RCA+ (from left to right) for the Villelongue real image.

We observe that the results obtained with both methods are in good visual agreement and highlight spatial structures that can be easily identified in the colour image (e.g., path) where one would expect nonlinear mixing to occur. More importantly, by not constraining the number of nonlinearity levels, G-RCA and G-RCA+ produce spatially smooth estimates that are realistic (and that do not require specification of the number of nonlinearity levels a priori). It is important to note that the results obtained with G-RCA+ indicate that the nonlinear effects in the image are sparser and weaker than previously suggested by RCA (and G-RCA). Due to the high correlation between the nonlinear terms (cross-products of the endmembers) as well as their energy, the estimation of the nonlinear coefficients is difficult, particularly for RCA and G-RCA that do not take into account the positivity of Γ . Indeed, in the model used in RCA and G-RCA Γ can take large positive and negative values which average out, leading to large estimated nonlinearity levels. By constraining the nonlinear coefficients to be non-negative, G-RCA+ yields smaller and sparser nonlinearity levels that are arguably closer to the ground truth. Finally, Figs. 5(e)–(f) show the estimated posterior probability of nonlinear mixing computed using (14) (with $\eta = 2$) and the nonlinear mixing detection results (computed by thresholding the probabilities w.r.t. 0.5). Again, nonlinearly mixed pixels are clearly identified near the path and at the boundary between two fields where we expect nonlinear mixing to occur.

The abundance maps obtained by G-RCA/G-RCA+ have been compared to those obtained with the algorithm considered in Section V and the results obtained by the different methods

are generally similar. As an example, Fig. 6 shows that the abundances estimates obtained with RCA, G-RCA, G-RCA+ (RCA-based nonlinear models) and with the NCLS (LMM-based) algorithm. Note that there is no abundance ground truth for this image making it difficult to quantify abundance estimation precision directly. This figure shows that algorithm based on the RCA model provide abundance maps generally in agreement with those obtained with NCLS, although the results can vary locally (e.g. abundances of the first endmember between the two fields). We implemented G-RCA(+) using $N_{MC} = 2000$ and $N_{bi} = 1500$ (computing these results using MATLAB required 7 hours on a 3 GHz Intel Xeon quad-core workstation). We observe that G-RCA and G-RCA+ perform similarly to the RCA algorithm, while not requiring fixing a number of classes. Finally, for this image all the methods achieved the same reconstruction error $RE = \sqrt{(\sum_{i,j} \|\hat{\mathbf{y}}_{i,j} - \mathbf{y}_{i,j}\|^2) / (N_{row} N_{col} L)} = 0.22$, due to the fact that the image is predominantly composed of linearly mixed pixels for which the eight methods perform similarly.

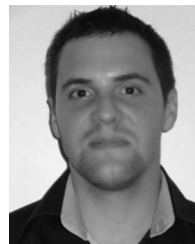
VII. CONCLUSION

This paper has presented a new hierarchical Bayesian algorithm for spectral unmixing of hyperspectral images which incorporates the spatial dependencies inherent in an image associated with the nonlinear mixture effects. The nonlinear mixtures were decomposed into a linear combination of the endmembers and an additive term which represents the nonlinear effects. This term was further decomposed as a

combination of the endmembers cross-products. A Gamma Markov random field was introduced to promote smooth non-linearity variations in the image. In contrast with previously reported work where nonlinear unmixing relied on a nonlinearity level-based image segmentation, the proposed model allows the level of nonlinearity to differ in each pixel while allowing the identification of regions where nonlinear effects occur. In this paper, a zero-mean Gaussian prior, restricted to the positive orthant was assigned to the nonlinear coefficients of each pixel. This choice was motivated by the fact that several existing models include positivity constraints for the nonlinear terms, e.g. [4]–[6], include such constraints within the SU procedure, and this was previously not possible using the RCA model in [11] due to the marginalisation of these parameters. The results presented in this paper have shown that it can significantly improve the unmixing performance. In this paper, the endmembers were assumed to be perfectly known but often need to be extracted from the data. Future work will include the generalisation of the G-RCA+ model to account for endmember estimation errors and more general sources of nonlinearity (such as endmember intrinsic variability). Finally, in some images abundances exhibit strong spatial correlations, and taking this information into account may improve estimation performance significantly [15], [26], [27]. Therefore it would be very interesting to design new models and nonlinear unmixing procedures that are capable of simultaneously exploiting the spatial correlations between abundances and between nonlinearities to produce best results.

REFERENCES

- [1] D. C. Heinz and C.-I. Chang, "Fully constrained least-squares linear spectral mixture analysis method for material quantification in hyperspectral imagery," *IEEE Trans. Geosci. Remote Sens.*, vol. 29, no. 3, pp. 529–545, Mar. 2001.
- [2] J. M. Bioucas-Dias *et al.*, "Hyperspectral unmixing overview: Geometrical, statistical, and sparse regression-based approaches," *IEEE J. Sel. Topics Appl. Earth Observ. Remote Sens.*, vol. 5, no. 2, pp. 354–379, Apr. 2012.
- [3] B. W. Hapke, "Bidirectional reflectance spectroscopy. I. Theory," *J. Geophys. Res.*, vol. 86, pp. 3039–3054, 1981.
- [4] B. Somers *et al.*, "Nonlinear hyperspectral mixture analysis for tree cover estimates in orchards," *Remote Sens. Environ.*, vol. 113, no. 6, pp. 1183–1193, 2009.
- [5] J. M. P. Nascimento and J. M. Bioucas-Dias, "Nonlinear mixture model for hyperspectral unmixing," in *Proc. SPIE Image Signal Process. Remote Sens. XV*, 2009, vol. 7477, p. 74770I.
- [6] A. Halimi, Y. Altmann, N. Dobigeon, and J.-Y. Tourneret, "Nonlinear unmixing of hyperspectral images using a generalized bilinear model," *IEEE Trans. Geosci. Remote Sens.*, vol. 49, no. 11, pp. 4153–4162, Nov. 2011.
- [7] I. Meganem, P. Deliot, X. Briottet, Y. Deville, and S. Hosseini, "Linear-quadratic mixing model for reflectances in urban environments," *IEEE Trans. Geosci. Remote Sens.*, vol. 52, no. 1, pp. 544–558, Jan. 2014.
- [8] J. Chen, C. Richard, and P. Honeine, "Nonlinear unmixing of hyperspectral data based on a linear-mixture/nonlinear-fluctuation model," *IEEE Trans. Signal Process.*, vol. 61, no. 2, pp. 480–492, Jan. 15, 2013.
- [9] Y. Altmann, A. Halimi, N. Dobigeon, and J.-Y. Tourneret, "Supervised nonlinear spectral unmixing using a postnonlinear mixing model for hyperspectral imagery," *IEEE Trans. Image Process.*, vol. 21, no. 6, pp. 3017–3025, Jun. 2012.
- [10] Y. Altmann, N. Dobigeon, and J.-Y. Tourneret, "Unsupervised postnonlinear unmixing of hyperspectral images using a Hamiltonian Monte Carlo algorithm," *IEEE Trans. Image Process.*, vol. 23, no. 6, pp. 2663–2675, Jun. 2014.
- [11] Y. Altmann, N. Dobigeon, S. McLaughlin, and J.-Y. Tourneret, "Residual component analysis of hyperspectral images—Application to joint nonlinear unmixing and nonlinearity detection," *IEEE Trans. Image Process.*, vol. 23, no. 5, pp. 2148–2158, May 2014.
- [12] A. Kalaitzis and N. D. Lawrence, "Residual components analysis," in *Proc. Int. Conf. Mach. Learn. (ICML)*, 2012, pp. 209–216.
- [13] O. Dikmen and A. T. Cemgil, "Gamma Markov random fields for audio source modeling," *IEEE Trans. Audio Speech Lang. Process.*, vol. 18, no. 3, pp. 589–601, Mar. 2010.
- [14] W. Fan, B. Hu, J. Miller, and M. Li, "Comparative study between a new nonlinear model and common linear model for analysing laboratory simulated-forest hyperspectral data," *Remote Sens. Environ.*, vol. 30, no. 11, pp. 2951–2962, Jun. 2009.
- [15] O. Eches, N. Dobigeon, and J.-Y. Tourneret, "Enhancing hyperspectral image unmixing with spatial correlations," *IEEE Trans. Geosci. Remote Sens.*, vol. 49, no. 11, pp. 4239–4247, Nov. 2011.
- [16] J. M. P. Nascimento and J. M. Bioucas-Dias, "Hyperspectral unmixing based on mixtures of dirichlet components," *IEEE Trans. Geosci. Remote Sens.*, vol. 50, no. 3, pp. 863–878, Mar. 2012.
- [17] M. Pereyra, N. Whiteley, C. Andrieu, and J.-Y. Tourneret, "Maximum marginal likelihood estimation of the granularity coefficient of a Potts-Markov random field within an MCMC algorithm," in *Proc. IEEE-SP Workshop Stat. Signal Process.*, Gold Coast, Australia, Jul. 2014, pp. 121–124.
- [18] M. Pereyra, N. Dobigeon, H. Batatia, and J.-Y. Tourneret, "Estimating the granularity coefficient of a Potts-Markov random field within an MCMC algorithm," *IEEE Trans. Image Process.*, vol. 22, no. 6, pp. 2385–2397, Jun. 2013.
- [19] C. P. Robert and G. Casella, *Monte Carlo Statistical Methods*, 2nd ed. Berlin, Germany: Springer-Verlag, 2004.
- [20] A. Pakman and L. Paninski, "Exact Hamiltonian Monte Carlo for truncated multivariate Gaussians," *J. Comput. Graph. Stat.*, 23, no. 2, pp. 518–542, 2014.
- [21] RSI (Research Systems Inc.), *ENVI User's Guide Version 4.0*. Boulder, CO, USA: RSI, Sep. 2003.
- [22] O. Eches, N. Dobigeon, and J.-Y. Tourneret, "Estimating the number of endmembers in hyperspectral images using the normal compositional model an hierarchical bayesian algorithm," *IEEE J. Sel. Topics Signal Process.*, vol. 3, no. 3, pp. 582–591, Jun. 2010.
- [23] D. Sheeren, M. Fauvel, S. Ladet, A. Jacquin, G. Bertoni, and A. Gibon, "Mapping ash tree colonization in an agricultural mountain landscape: Investigating the potential of hyperspectral imagery," in *Proc. IEEE Int. Conf. Geosci. Remote Sens. (IGARSS)*, Jul. 2011, pp. 3672–3675.
- [24] Y. Altmann, N. Dobigeon, S. McLaughlin, and J. Tourneret, "Nonlinear spectral unmixing of hyperspectral images using Gaussian processes," *IEEE Trans. Signal Process.*, vol. 61, no. 10, pp. 2442–2453, May 2013.
- [25] J. M. P. Nascimento and J. M. Bioucas-Dias, "Vertex component analysis: A fast algorithm to unmix hyperspectral data," *IEEE Trans. Geosci. Remote Sens.*, vol. 43, no. 4, pp. 898–910, Apr. 2005.
- [26] M.-D. Iordache, J. M. Bioucas-Dias, and A. Plaza, "Total variation spatial regularization for sparse hyperspectral unmixing," *IEEE Trans. Geosci. Remote Sens.*, vol. 50, no. 11, pp. 4484–4502, Nov. 2012.
- [27] J. Chen, C. Richard, and P. Honeine, "Nonlinear estimation of material abundances in hyperspectral images with ell_1 -norm spatial regularization," *IEEE Trans. Geosci. Remote Sens.*, vol. 52, no. 5, pp. 2654–2665, May 2014.



Yoann Altmann (S'10–M'14) was born in Toulouse, France, in 1987. He received the Engineering degree in electrical engineering from Ecole Nationale Supérieure d'Electronique, d'Electrotechnique, d'Informatique, d'Hydraulique et des Télécommunications, Toulouse, France, the M.Sc. degree in signal processing from the National Polytechnic Institute of Toulouse (INP Toulouse), Toulouse, France, both in 2010, and the Ph.D. degree from INP Toulouse, INP Toulouse, in 2013. Since 2014, he has been with the Heriot-Watt University, Edinburgh, U.K., as a Postdoctoral Researcher. He conducts his research within the Institute of Sensors, Signals, and Systems, School of Engineering and Physical Sciences. His research interests include statistical signal and image processing, with a particular interest in Bayesian inverse problems with applications to remote sensing, and biomedical imaging.



Marcelo Pereyra (S'09–M'13) was born in Buenos Aires, Argentina, in 1984. He received the M.Eng. degree in electronic engineering from both ITBA, Buenos Aires, Argentina, and INSA Toulouse, Toulouse, France, the M.Sc. degree from INSA Toulouse, and the Ph.D. degree in signal processing from the Institut National Polytechnique de Toulouse, University of Toulouse, Toulouse, France, in 2009 and 2012, respectively. He currently holds a Marie Curie Research Fellowship at the School of Mathematics, University of Bristol, Bristol, U.K. His

research interests include centred around statistical image processing with a particular interest in Bayesian inference and computation for high-dimensional inverse problems.



Steve McLaughlin (F'11) was born in Clydebank, Scotland, in 1960. He received the B.Sc. degree in electronics and electrical engineering from the University of Glasgow, Glasgow, U.K., and the Ph.D. degree from the University of Edinburgh, Edinburgh, U.K., in 1981 and 1990, respectively. From 1981 to 1984, he was a Development Engineer in industry involved in the design and simulation of integrated thermal imaging and fire control systems. From 1984 to 1986, he worked on the design and development of high frequency data communication systems. In

1986, he joined the Department of Electronics and Electrical Engineering, University of Edinburgh, as a Research Fellow, where he studied the performance of linear adaptive algorithms in high noise and nonstationary environments. In 1988, he joined the Academic Staff at Edinburgh, and from 1991 to 2001, he held a Royal Society University Research Fellowship to study nonlinear signal processing techniques. In October 2011, he joined Heriot-Watt University, Edinburgh, U.K., as a Professor of signal processing and Head of the School of Engineering and Physical Sciences. His research interests include adaptive signal processing and nonlinear dynamical systems theory and their applications to biomedical, and energy and communication systems. In 2002, he was the Personal Chair in Electronic Communication Systems, University of Edinburgh. He is a Fellow of the Royal Academy of Engineering, Royal Society of Edinburgh, and Institute of Engineering and Technology.